ACS Photonics

pubs.acs.org/journal/apchd5

Article

Integrated PbS Colloidal Quantum Dot Photodiodes on Silicon Nitride Waveguides

Chao Pang, Yu-Hao Deng, Ezat Kheradmand, Nithin Poonkottil, Robin Petit, Lukas Elsinger, Christophe Detavernier, Pieter Geiregat, Zeger Hens, and Dries Van Thourhout*

Cite This: https://doi.org/10.1021/acsphotonics.3c00945

Read Online

ACCESS | Metrics & More | Article Recommendations | Supporting Information

ABSTRACT: Colloidal quantum dots (QDs) have become a versatile optoelectronic material for emitting and detecting light that can overcome the limitations of a range of electronic and photonic technology platforms. Photonic integrated circuits (PICs), for example, face the persistent challenge of combining active materials with passive circuitry ideally suited for guiding light. Here, we demonstrate the integration of photodiodes (PDs) based on PbS QDs on silicon nitride waveguides (WG). Analyzing planar QDPDs first, we argue that the main limitation WG-coupled QDPDs face is detector saturation induced by the high optical power density of the guided light. Using the cladding thickness and waveguide width as design parameters, we mitigate this issue, and we demonstrate WG-QDPDs with an external quantum efficiency of 67.5% at 1275 nm that exhibit a linear photoresponse for input powers up to 400 nW. In the next step, we demonstrate a compact infrared spectrometer by integrating these WG-QDPDs on the output channels of an arrayed waveguide grating demultiplexer. This work provides a path toward a low-cost PD solution for PICs, which are attractive for large-scale production.

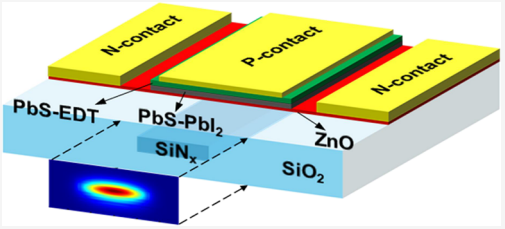

KEYWORDS: *colloidal quantum dots, photodiode, waveguide, silicon nitride, photonics integration*

INTRODUCTION

Colloidal quantum dots (QDs) are emerging as a promising class of semiconductors for a wide range of optoelectronic applications. Examples including light emitting diodes (LED),[1,2] lasers,[3−5] solar cells,[6] and photodetectors[7,8] are enabled by QDs offering a combination of an efficient emission and pronounced absorption tunable from visible to infrared wavelengths,[9] low-cost chemical synthesis, solution-based processing, and compatibility with different substrates.[10] Following the rapid material development and the improved understanding of QD-based devices,[9] interest is moving to the integration of QDs in established optoelectronic technology platforms. QDs have, for example, been included as color convertors in liquid crystal and micro-LED displays[11,12] and combined with a driver backplane for electroluminescent displays[13,14] or a readout backplane for infrared imagers.[15,16] QDs can be equally attractive for integration with photonic integrated circuits (PICs), where the low cost, ease of processing, and compatibility with a wide range of substrates are appealing with respect to other integration approaches. Indeed, while the monolithic epitaxial growth of semiconductors on PICs has the advantage of high throughput and low cost, substrate compatibility remains a major challenge.[17] Heterogeneous integration technology based on wafer or die bonding is well developed and has led to commercial products, but the approach requires large-area planarized surfaces and makes use of costly III−V epitaxy and bonding technology.[18,19] Assembly-based hybrid integration technologies, such as flip-chip integration and transfer printing, offer excellent compatibility between diverse material platforms, yet complex processing and throughput remain to be demonstrated.[18,20,21]

Silicon nitride (SiN) is a promising integrated photonics platform characterized by a low propagation loss, high power handling capability, a broad transparency window, and compatibility with processing in CMOS fabs.[22] Applications of SiN-based integrated photonics range from lidar[23−25] to biosensing[26−28] and quantum photonics.[29−31] However, the integration of active components into SiN remains a challenge. Leveraging their excellent substrate compatibility and patterning flexibility, solution-processed materials have been introduced into the SiN photonics platform for different purposes, for example, as gain material for lasers[4,32,33] and as single photon emitter.[34−36] However, most of these devices are driven optically. Integration in SiN of electrically driven devices, such as infrared (IR) photodetectors, has only been achieved by heterogeneous or hybrid methods involving

Received: July 7, 2023

bonding[37] or transfer printing.[38] Given the limitations of these approaches mentioned above, QD-based photodiodes (QDPDs) offer an appealing alternative for IR detection on SiN.

Building on extensive research into QD solar cells, current IR-sensitive QDPDs based on PbS QDs can attain an external quantum efficiency (EQE) of 80%,[7] a response time of 10 ns[7], a dark current density of 2.9×10^{-5} mA cm^{-2}, and a detectivity of 6.7×10^{12} Jones at 980 nm.[39] Moreover, spectral sensitivity has been demonstrated up to 1.55 μm[7] and even up to 3 μm.[40] These levels of efficiency and detectivity have led to the first commercial introduction of IR imagers based on a PbS QDPDs pixel array.[15] A similar integration of distinct QDPDs on PICs could enable complex functionality, such as pocket spectrometers for sensing or compact wavelength division multiplexing (WDM) receivers for datacom applications. However, the integration of QDPDs on waveguides and PICs is still in its infancy. A first prototype involving a CdSe QDPD on a SiN waveguide was demonstrated by Elsinger et al., but this QDPD was only sensitive to visible light, had a modest external quantum efficiency of 6% at best, and featured a strongly sublinear response to light intensity.[41] Clearly, such issues need to be addressed for QDPDs to become widely deployed as IR detectors on SiN-integrated photonics.

In this work, we demonstrate the integration in SiN waveguides of a QDPD consisting of two films of PbS QDs, with surfaces functionalized by lead iodide (PbI_2) and ethanedithiol (EDT), respectively, stacked on a ZnO electron transport layer. After analyzing the power-dependent saturation of the photocurrent by means of a bottom-illuminated, planar QDPD, we first map the design parameters of an integrated QDPD that would ensure a linear power response at relevant power levels. Next, we show that the relatively simple three-layer QDPD stack can be integrated on SiN strip waveguides. Using a waveguide width and cladding thickness that keeps the QDPD operating within the linear regime, we show a responsivity of 0.69 A/W, corresponding to an EQE of ~67.5% at 1275 nm, and a linear response for illumination powers up to 400 nW at −1 V bias. Interestingly, this EQE is significantly better than that of the planar stack, probably due to the better absorbance of light incident parallel to the surface of the integrated QDPD. As a final step, we demonstrate a QDPD array integrated with an eight-channel arrayed waveguide grating (AWG) demultiplexer, which works as a compact infrared spectrometer. This first demonstration of integrating multiple QDPDs to create an on-chip spectroscopic system provides a promising route for mass integration of QDPDs in complex photonic ICs applicable in a wide range of applications.

RESULTS AND DISCUSSION

Formation and Characterization of PbS Quantum Dot Photodiodes. On-chip waveguides can be very compact with a typical cross-sectional area below 1 μm^2. The ensuing strong optical confinement increases the power density and the carrier generation rate within a photoactive layer positioned on top of the waveguide, possibly leading to photodetector saturation. In literature, analysis of QDPDs is mostly carried out at relatively low power levels, that is, lower than 100 mW/cm^2.[42,43] Few studies, if any, have addressed the power-dependent saturation of QDPDs. To assess the limits of a linear photoresponse, we first analyzed planar bottom-illuminated QDPDs (BI-QDPDs). These devices consisted of a stack of 100 nm ITO-on-glass, 50 nm ZnO, 60 nm PbS-PbI_2, 60 nm PbS-EDT, and 100 nm Au; see Figure 1a. The *n*-doped

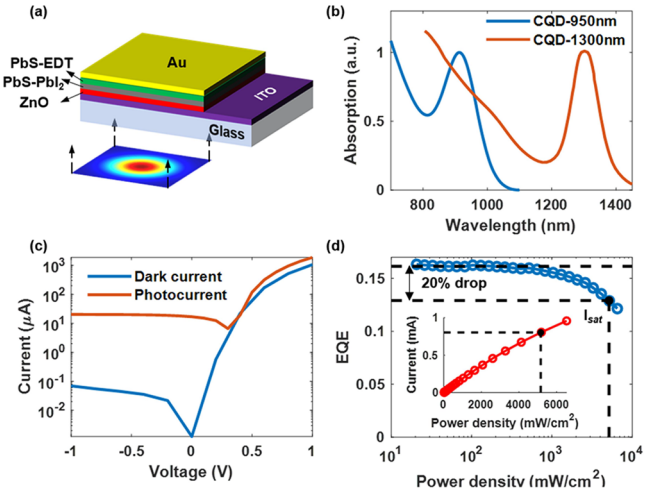

Figure 1. Structure and characterization of BI-QDPD. (a) Device structure of the BI-QDPD, illuminated from the bottom glass side by laser with Gaussian beam shape. (b) Absorption spectra for both types of QDs used in the BI-QPDD, dispersed in *n*-octane. QDs with the exciton peak around 1300 nm were used for absorption, and QDs around 950 nm were used as hole-transport and electron-blocking materials. (c) Dark current and photocurrent of BI-QDPD with an area of 1.77 mm^2. The photocurrent was measured for illumination at 1275 nm with a power of 0.16 mW (peak power density of ~100 mW/cm^2). (d) EQE of BI-QDPD vs optical power density at a bias voltage of −1 V. The intersection of the dashed lines indicates the onset of saturation. Inset: photocurrent vs optical maximum power density. The optical power density is measured in the center of the Gaussian beam illuminating the BI-QDPD.

ZnO-film, formed using a sol−gel process, acts as an electron transport and hole-blocking layer, while the specifications PbI_2 and EDT refer to layers of as-synthesized QDs that had a surface treatment with lead iodide and ethanedithiol, respectively. According to the literature, these treatments enhance charge-carrier mobility and result in PbS QD films with *n*-type and *p*-type characters, respectively.

In practice, the exchange of the long lead oleate ligands by PbI_2 was accomplished through solution-phase ligand exchange,[44] while the EDT surface treatment involved a solid-phase ligand exchange. Importantly, as shown in Figure 1b, the PbS-PbI_2 and PbS-EDT layers consisted of QDs with a band gap absorption at 1300 and 950 nm, respectively. In this way, the first layer serves as the absorber layer for light with wavelengths up to 1300 nm, while the second layer acts as the hole transport layer. Finally, the PbS-EDT layer was contacted by a gold film thermally evaporated using a shadow mask. According to the literature, such a heterogeneous stack of PbS-EDT/PbS-PbI_2/ZnO forms a p−i−n junction, where the 60 nm absorption region of PbS-PbI_2 is fully depleted.[45] Additional details on the QD synthesis and the BI-QDPD fabrication can be found in the Methods section.

To analyze the photoresponse of the BI-QDPD, we illuminated the device using a 1275 nm laser beam with a Gaussian beam profile and variable total incident power; see Figure 1a. Because of this inhomogeneous illumination profile, we quantified the photoresponse by means of the photocurrent, rather than the photocurrent density. Accordingly, Figure 1c represents the current/voltage characteristics of a

https://doi.org/10.1021/acsphotonics.3c00945
ACS Photonics XXXX, XXX, XXX−XXX

typical BI-QDPD. In the dark, we observed a pronounced diode behavior with a dark current of 70 nA—corresponding to a dark current density of ~4 μA/cm^2—at a bias voltage of −1 V (Figure 1c). In addition, we measured a nearly constant photocurrent under reverse bias upon illumination, which we believe reflects the efficient extraction of photogenerated carriers from the PbS-PbI$_2$ layer. Quantitatively, we obtained a photocurrent of 0.02 mA for a total illumination power of 0.12 mW, corresponding to an external quantum efficiency (EQE) of 16%, where EQE is defined as the ratio of the number of collected photogenerated carriers and the number of incident photons. Figure 1d displays the EQE of the BI-QDPD measured at a bias voltage of −1 V as a function of the peak power density of the laser, where a total power of 0.12 mW corresponds to a peak power density of 100 ± 10 mW/cm^2. As can be seen, a transition occurs from a constant EQE of 16% to a regime where the EQE drops with increasing power density, which implies that at such power densities, the photocurrent no longer increases linearly with the incident power. To quantify this saturation effect, we define the saturation power density I_{sat} as the power density at which the EQE drops by 20% from its initial value (averaged EQE for power density <400 mW/cm^2). Figure 1d shows that I_{sat} defined in this way amounts to 5.2 W/cm^2, which we will take as a reference for the design of a WG-QDPD that operates in the linear regime at relevant power levels.

Design of Waveguide-Integrated Quantum Dot Photodiodes. Our aim was to realize an evanescently coupled QDPD (WG-QDPD) by fabricating the device stack on top of a 300 nm thick SiN waveguide layer; see Figure 2a. Such a configuration offers multiple design parameters to adjust the power density in the absorbing layer and thus maximize the optical power of the guided light at which detector saturation occurs. In this study, we limited the parameter space to the waveguide width w and the cladding thickness t. Wider waveguides limit the power density of the guided light, while increasing the separation between the top of the SiN waveguide and the QDPD stack reduces the overlap of the evanescent optical field with the QDPD.

Different from the BI-QDPD, illumination occurs parallel to the PbS QD films in the WG-QDPD design proposed in Figure 2a. To use the saturation power density of ~5.2 W/cm^2 measured on a BI-QDPD as a design constraint in this different geometry, we started from the notion that carrier extraction still occurs in the same vertical (z) direction for both QDPDs. Hence, when splitting the PbS-PbI$_2$ absorber layer into small cells parallel to the z-direction, as shown in Figure 2b, the total carrier generation in each cell will determine a concomitant local saturation. For both QDPDs, it is the cell with the highest total generation rate that determines the onset of saturation of the entire QDPD. As depicted in Figure 2b, this is the cell in the center of the film for the BI-QDPD, while it is the central cell at the edge of the film for the WG-QDPD, as depicted in Figure 2b.

In general, the maximum carrier generation rate Γ_{max} across the different cells in a given film can be calculated as

$$\Gamma_{max} = \max[\Gamma(x, y)] = \max\left[\int G(x, y, z)dz\right] \quad (1a)$$

$$G(x, y, z) = \frac{P_{abs}(x, y, z)}{h\nu} = \frac{2\pi n\kappa\varepsilon_0}{h}|E(x, y, z)|^2 \quad (1b)$$

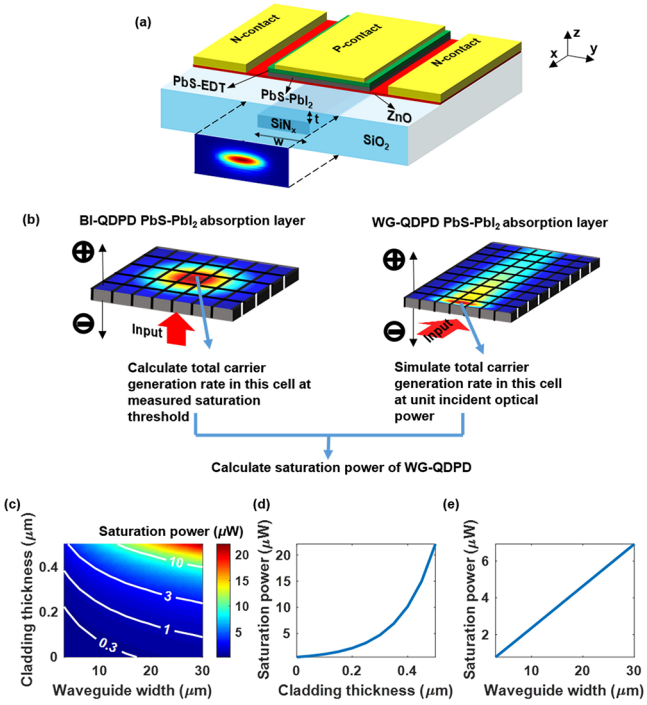

Figure 2. Design of WG-QDPD. (a) Device structure of WG-QDPD. (b) Link between saturation of BI-QDPD and WG-QDPD. Red arrows point out the light propagation direction, vertical for the BI-QDPD and horizontal for the WG-QDPD. The electrons and holes are extracted in the vertical direction for both cases. The PbS-PbI$_2$ absorption layer can be split into small cells. The total carrier generation rate in each cell determines its local saturation. The cell with the maximum total carrier generation rate (indicated by a blue arrow) determines the onset of saturation for the whole PD. (c) Simulated saturation power of WG-QDPD vs cladding thickness and waveguide width. (d) Slice of (c) for a waveguide width of 30 μm. (e) Slice of (c) for a cladding thickness of 0.35 μm.

Here, $G(x, y, z)$ is the carrier-generation rate (units m^{-3}s^{-1}) at a specific point in the film, while $\Gamma(x, y)$ is the integrated carrier-generation rate along the z-direction. In addition, $P_{abs}(x, y, z)$ is the optical power absorbed per unit volume, $h\nu$ is the photon energy, ε_0 is the vacuum permittivity, n and κ are the real and imaginary parts of the complex refractive index of the PbS-PbI$_2$ film respectively, and $E(x, y, z)$ is the electrical field. Note that we considered the *z-integrated* generation rate, rather than the (x, y, z) point generation rate. This approach assumes that the actual distribution of the carrier generation rate in the z-direction has minimal influence on the carrier extraction, a reasonable consideration since the QD absorber layer utilized here is thin enough to consider a uniform built-in electrical field for carrier extraction throughout the absorber layer.

Given the measured saturation power density of 5.2 W/cm^2 of the BI-QDPD, we estimated the threshold Γ_{max} at 3 × 10^{22} m^{-2}s^{-1}; see Supporting Information S1. Using a finite difference eigenmode solver (Lumerical), we simulated the electric field in the QD films, from which we obtained Γ_{max} of the WG-QDPD for a unit of incident optical power, as shown in Supporting Information S1. By keeping Γ_{max} at the threshold value of 3 × 10^{22} m^{-2} s^{-1}, we then mapped the optical power of the guided light at which the WG-QDPD will saturate as a function of the waveguide width and the cladding thickness. As shown in Figure 2c–e, we found that the saturation power

https://doi.org/10.1021/acsphotonics.3c00945
ACS Photonics XXXX, XXX, XXX−XXX

increases exponentially with cladding thickness, an outcome that reflects the exponential decay of the evanescent tail of the waveguide mode and increases linearly with waveguide width, in agreement with the linear extension of the optical mode. Note, however, that to keep the fraction of absorbed light constant, a lowering of the power density in the absorbing layer will come at the expense of a longer QDPD, which will increase the dark current without yielding more photocurrent.

For a single-mode waveguide with a width of 1 μm and no top cladding, the calculated saturation power is as low as 28 nW. On the other hand, a combination of a top cladding thickness of 350 nm and a waveguide width of 30 μm should yield a saturation power of up to 6.9 μW. For these design parameters, we estimated the loss of the waveguide functionalized with the WG-QDPD stack at 623 dB/cm, of which 87% involves absorption of light within the PbS-PbI_2 QDs and the remainder mostly related to absorption within the ZnO layer and the metal top contact. As a result, a 200 μm long WG-QDPD is needed to absorb 95% of the input light, with a maximally attainable EQE of 82%. This design targets the fundamental TE mode. However, given the large waveguide width utilized and potential perturbations, guided light could couple into higher-order TE modes or even TM modes. Nonetheless, our simulations indicate that there is no obvious change (<0.3%) in terms of optical loss and attainable EQE for the 10 lowest order TE-like modes. TM modes exhibit a higher optical loss of 1432 dB/cm, yet a similar attainable EQE of 77%. We thus conclude that the proposed integrated QDPD design can achieve efficient light absorption and stable performance. According to the dark current density recorded on the BI-QDPD, such a WG-QDPD would have a dark current of 0.3 nA, which is considerably smaller than the expected photocurrent. Since further increasing the cladding thickness or waveguide width will deteriorate the trade-off between power saturation and dark current, we settled for a waveguide width of 30 μm and a top cladding thickness of 350 nm to demonstrate the first generation of WG-QDPDs.

Fabrication of WG-QDPDs. Figure 3 represents the process flow we used to fabricate WG-QDPDs. In short,

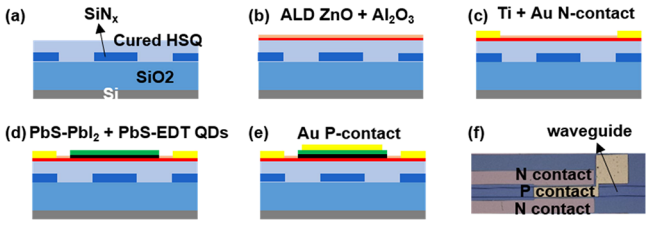

Figure 3. Processing steps to fabricate WG-QDPD. (a) SiN waveguide patterning and top cladding deposition. (b) ALD of the ZnO electron transport layer and Al_2O_3 protection layer. (c) N-contact metal patterning with photoresist and liftoff. (d) QD film patterning with PMMA resist and liftoff. The Al_2O_3 protection layer was removed before spin-coating QDs. (e) P-contact metal patterning with PMMA resist and liftoff. (f) Top view of the fabricated WG-QDPD.

starting from a silicon substrate with a 3 μm thermal oxide, we first deposited a 300 nm thick SiN layer by plasma-enhanced chemical vapor deposition (PECVD). Next, the SiN waveguides were patterned using electron beam lithography (EBL) with a positive resist, followed by reactive ion etching (RIE) with CF_4 and H_2 chemistry. To planarize the sample, the flowable oxide hydrogen silsesquioxane (HSQ) was spun on top, followed by curing at 400 °C in N_2 for 2 h to increase its chemical stability (Figure 3a). Note that while we made use of lab-processed waveguides in this study, a similar integration approach could be used for integrating QDPDs on waveguides fabricated in a classical foundry process using DUV lithography and wafer scale processes.

To fabricate the actual WG-QDPDs, a 20 nm thick ZnO electron transport layer was first formed by using atomic layer deposition (ALD). As indicated in Figure 3b, the layer was topped by a 10 nm protective Al_2O_3 layer to prevent the ZnO from losing conductivity during exposure to oxygen plasma used for sample cleaning in the following steps. The ALD layer was annealed at 400 °C for 1 min in a N_2 and H_2 atmosphere to increase the conductivity of the ZnO. Photolithography and liftoff were used to pattern the *n*-contact, a process including the removal of the Al_2O_3 by a dilute KOH solution and the deposition of metal contacts consisting of 20 nm Ti and 100 nm Au; see Figure 3c. We then patterned the ZnO using photolithography and wet etching (dilute KOH to remove Al_2O_3, followed by dilute HCl to remove ZnO) and used EBL and liftoff to deposit a patterned QD film,[34] as shown in Figure 3d. Here, PMMA was used as a resist due to the chemical compatibility with the solvent used during the deposition of the QD film. Before depositing QDs, Al_2O_3 was removed by a hot dilute KOH solution to obtain a direct contact between the ZnO electron transport layer and the QD film. Similar to the case for the BI-QDPD, the QD film consisted of a sequence of an *n*-type PbS-PbI_2 and a *p*-type PbS-EDT layer. Finally, the PMMA was removed using liftoff in acetone, and a 100 nm thick Au *p*-contact was defined through EBL and liftoff; see Figure 3e. Figure 3f shows a top-view microscopy image of a fabricated WG-QDPD, in which all relevant parts have been highlighted. Using this approach, WG-QDPDs with different waveguide widths were fabricated on a single chip to confirm the predicted width-dependent saturation of the WG-QDPD. We also defined a WG-QDPD array on an eight-channel arrayed waveguide grating (AWG) to realize a more complicated functionality using WG-QDPDs. Reference waveguides without integrated QDPD were also included on the chip to calibrate the power coupled to the waveguides. Additional details on the fabrication of the WG-QDPD can be found in the Methods section.

Characterization of WG-QDPD. We characterized the WG-QDPDs using a source measurement unit (Keithley 2450), DC probes, and an O-band tunable laser. The light was coupled into the SiN waveguides through grating couplers. The optical power of the guided light was calibrated by measuring the coupling efficiency of the grating coupler for the reference waveguide without QDPDs; see Supporting Information S2. Figure 4a represents the current−voltage curves of a WG-QDPD in the dark and upon illumination with 1275 nm of light of various intensities. One sees that the dark current increases from the expected <1 nA at a low reverse bias to 2.4 nA at a −1 V bias. Possibly, this difference with the BI-QDPD is related to the different way of forming the *n*-ZnO layer in both cases, that is, through ALD for the WG-QDPD and through a sol−gel process for the BI-QDPD. On the other hand, a nearly constant photocurrent is obtained upon illumination. As shown in Figure 4b,c, the best devices showed linear responsivity and constant EQE at low illumination power. More precisely, an average EQE of 67.5% is obtained in the range of 6−60 nW, which drops to 54% at the saturation

https://doi.org/10.1021/acsphotonics.3c00945
ACS Photonics XXXX, XXX, XXX−XXX

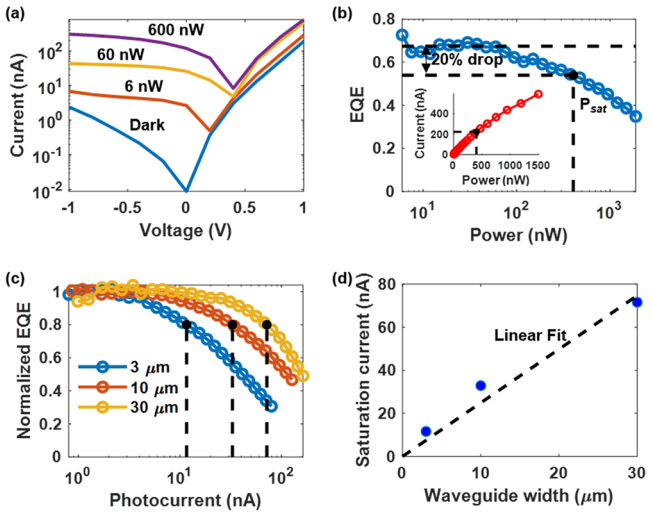

Figure 4. Response of WG-QDPDs. (a) *I*−*V* curves of WG-QDPDs under dark conditions and illumination at 1275 nm. (b) EQE vs optical power at −1 V bias voltage. Inset: photocurrent vs optical power with bias voltage of −1 V. The intersection of the black dashed lines indicates the onset of saturation. (c) Normalized EQE vs photocurrent at −2 V bias voltage for different waveguide widths. The saturation points of WG-QDPDs are indicated by vertical black dashed lines. (d) Saturation photocurrent with different waveguide widths. A linear fit is indicated by the black dashed line.

optical power (P_{sat}) of 400 nW, a 20% reduction that we took as marking the end of the linear regime. Note that this experimental result is about 1 order of magnitude smaller than the predicted saturation power of 6.9 μW, which was based on the characteristics of the BI-QDPD. Probably, this outcome reflects the differences between the idealized structure used for the simulations, and the actually formed WG-QDPD, which can accumulate contamination and defects during the different fabrication steps. Even so, we do retrieve the expected variation of the saturation behavior of the WG-QDPDs with varying waveguide widths, for which we characterized saturation by the measured photocurrent rather than the optical power so as to circumvent possible measurement errors induced by variations of the optical coupling efficiency; see Figure 4c. Notably, WG-QDPDs with different waveguide widths, increasing from 3 to 10 and 30 μm, exhibited the predicted proportional increase in saturation power as the optical power intensity in the absorbing layer decreased; see Figure 4d. We, therefore, conclude that a PbS-based QDPD stack can be successfully integrated on SiN waveguides and that the issue of detector saturation can be mitigated by the design parameters of the WG-QDPD, such as the waveguide width.

Formation of an Integrated QD Spectrometer. To illustrate what our approach of integrating QDPDs can accomplish, we fabricated a set of WQ-QDPDs on the output channels of an arrayed waveguide grating (AWG), which can work as a compact spectrometer. The AWG was designed with IPKISS[46] and fabricated on a single chip together with the passive waveguides discussed above, see Figure 5a. The AWG was designed to have a free spectral range (FSR) of 60 nm, splitting the light into eight wavelength channels with a spacing of 7.5 nm. We characterized the spectral response of this compact spectrometer by injecting monochromatic light, tuned in wavelength from 1260 to 1320 nm, from the input grating coupler, and measured the photocurrent in each channel

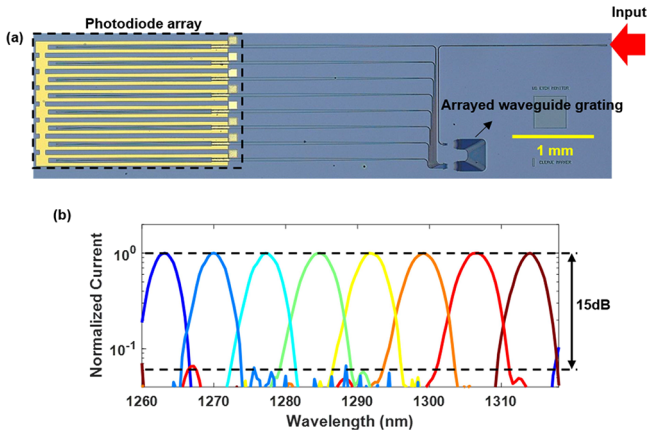

Figure 5. Integrated spectrometer with a QDPD array and AWG. (a) Top view of the spectrometer. Light is injected from the right grating coupler. (b) Response of eight channels without applying bias voltage. The response of each channel was normalized to its maximum.

without applying a bias voltage. Figure 5b presents the normalized photocurrent in each channel. One sees that sweeping the wavelength indeed leads to a photoresponse in the different WQ-QDPDs. In line with the design specifications, the 8-band spectrometer covers a wavelength range of 51 nm, corresponding to a channel spacing of 7.3 nm. The measured channel crosstalk was better than 15 dB, which is sufficient for many applications. This crosstalk is limited by phase errors in the dispersive waveguide array introduced during the fabrication. It has been shown that by optimizing the design and processing, for example, by using DUV lithography instead of electron beam lithography, these phase errors can be minimized and crosstalk values up to 30 dB can be readily achieved.[47,48] Moreover, the AWG design can be adapted to meet the requirements of given applications. To reach a higher resolution, the channel spacing can be reduced, or more channels can be added. Alternatively, in data applications, the AWG can be designed with a flat channel response instead of a Gaussian shape, by using multimode interference couplers as input apertures.[49] This demonstrates the flexibility of this on-chip approach and opens up its use in many different applications such as in vivo glucose monitoring[50,51] and fiber Bragg grating readout.[52]

DISCUSSION

Most of the photodetectors integrated on SiN waveguides reported in literature were based on bonded or transfer-printed III−V semiconductors,[37,53] Ge monolithically grown on Si,[54,55] and two-dimensional materials,[56,57] approaches that result in increased integration complexity. Integration of evaporated amorphous[58] and polycrystalline[59] photoconductors has also been demonstrated, offering promising pathways for less complex heterogeneous integration. However, such photoconductors have been associated with the observation of a notable dark current and low detectivity,[58,59] attributed to the inherent photoconductor mechanism. Here, we have demonstrated the formation of QD-based photodiodes on SiN waveguides by means of standard film deposition and patterning techniques. These WG-QDPDs exhibit a lower dark current (2.4 nA at −1 V) than most of the previously demonstrated photodetectors. In addition, our WG-QDPDs demonstrate a high responsivity of 0.69 A/W at around 1.3 μm, which is comparable to, or even better than, reported

https://doi.org/10.1021/acsphotonics.3c00945
ACS Photonics XXXX, XXX, XXX−XXX

waveguide-coupled PDs.[53,55,60] Moreover, the use of QDs as active material offers the benefits of a low-cost material, compatibility with standard fabrication techniques, ease of processing, and scalability toward higher volume production. These features make WG-QDPDs attractive for low-cost, low-power, and noise-sensitive applications. Finally, planar QDPDs have been demonstrated to exhibit a response time as short as 10 ns.[7] However, this fast response time has been observed only in small pixel devices, indicating that the response time is primarily limited by the resistance-capacitance (RC) product. In this respect, WG-QDPDs, with their smaller active area and consequently reduced capacitance, hold great potential for achieving even faster response times. In more detail, the capacitance of our WG-QDPD is expected to approximate 15 pF, considering a dielectric constant of 34,[7] a device area of 6000 μm^2, and a QD layer thickness of 120 nm. With a load resistance of 50 Ω, the RC limited response time (10−90% rise time, calculated as 2.2·RC) is estimated to be 1.7 ns.

Although in this work E-beam lithography was used for patterning the QD layer and the p-contact metal, nothing prevents the use of photolithography as an alternative,[61,62] enabling the fabrication of WG-QDPDs on the wafer scale with high throughput. Furthermore, the process used to integrate PbS QDPDs on the SiN waveguide platform can be extended to other QD materials and photonic integrated platforms. For the silicon-on-insulator (SOI) platform, monolithically integrated Ge detectors are the preferred solution for wavelengths below 1.6 μm. However, for longer wavelengths, there is still no straightforward integrated solution. Larger PbS QDs can have absorption onsets beyond 2 μm, and other materials like HgTe QDs can even work in the mid-infrared range.[63,64] These QDs can be good candidates for integration on SOI or Ge-on-Si PIC platforms targeting longer wavelength ranges.[65,66] For other platforms such as flexible photonics, which meet with similar challenges of integrating active components, QDPDs are also a promising candidate.

While the saturation power of WG-QDPDs is better than that of two-dimensional materials photodetectors,[57] it is still not on par with III−V or Ge photodetectors, which have saturation powers exceeding 1 mW.[53,67] Hence, a significant enhancement of the saturation power is needed to make WG-QDPDs competitive in this way, a step that is contingent upon better fabrication techniques and the design and operation of the QDPD stack. For the fabrication, we believe that minimizing damage to the QD and transport material films, as well as ensuring cleaner interfaces, could significantly enhance the performance of WG-QDPDs, bringing them closer to that of planar QDPDs. For the QDPD stack, however, limited literature is available on the origin of the detector saturation. Possibly, the low saturation power of PbS QDPDs compared with epitaxial PDs, is related to a high series resistance induced by the low mobility of the QDs film. As a result, higher carrier densities are needed to sustain a given photocurrent. More generally, however, the results presented here call for a better understanding of detector saturation in QDPDs.

Benefiting from the wide tunability of the QD absorption spectrum, the concept of computational spectrometers based on the wavelength multiplexing principle[68] has emerged as a compelling option. In this scheme, hundreds of QDs, each characterized by a distinct absorption spectrum, function as specialized filters that randomly sample the desired spectrum. Subsequent computational techniques enable the reconstruction of the sampled data. A key departure from traditional spectrometers, including the one exemplified in our current study, is that the inherent trade-off between resolution and bandwidth becomes obsolete in the realm of computational spectrometry. The integration of QD-based computational spectrometers into integrated photonics also holds substantial promise. However, a series of potential challenges need to be overcome, such as the efficiency and yield concerns of multistep QD deposition, effectively controlling QD absorption behavior, and realizing low-loss and broadband power splitters.

CONCLUSIONS

In this work, we have demonstrated for the first time PbS QDPDs integrated on SiN waveguides using standard process techniques. Based on the characterization of planar QDPDs, we argue that the high optical intensity resulting from the strong optical confinement in waveguides could induce saturation of a WG-QDPD at low optical power. We overcome this issue through a design in which the WG-QDPD overlap is coupled to the evanescent field, while using the cladding thickness and the waveguide as adjustable parameters to raise the saturation power by reducing the overlap with the evanescent field. In particular, we demonstrate that a 30 μm wide device with a 350 nm cladding layer can exhibit a responsivity of 0.69 A/W and a linear response of up to 400 nW for 1275 nm light at a −1 V reverse bias. Such a combination, however, involves a trade-off between an increased saturation threshold and an enhanced dark current since longer detectors are needed to absorb a given fraction of the guided light. To further demonstrate the scalability of the integration approach proposed here, we also designed and tested a compact 8-channel spectrometer integrated with an array of WG-QDPDs. This spectrometer showed a clear wavelength-dependent response with a channel crosstalk of 15 dB. We believe that these results will inspire further research into the integration of colloidal active materials on PICs.

METHODS

Synthesis of 950 nm PbS QDs. Lead oleate and N-(3,5-bis(trifluoromethylphenyl))-*N*′-phenylthiourea were synthesized according to Hendricks et al.[69] In a three-neck flask, 7.00 mmol of lead oleate (5.38 g, 1.50 equiv) was dissolved in 25 mL of anhydrous *n*-octane at 90 °C under a nitrogen atmosphere. In a vial, 4.67 mmol of *N*-(3,5-bis-(trifluoromethylphenyl))-*N*′-phenylthiourea (1,70 g, 1 equiv) and 2 mL of 1-methoxy-2-(2-methoxyethoxy)ethaan were mixed and heated to 90 °C as well. The thiourea solution was then quickly injected into the lead oleate solution via a syringe, and the flask was cooled to room temperature by immersion into a water batch after 1 min. The resulting dispersion was purified four times with the aid of *n*-octane and acetone under ambient conditions and stored in anhydrous *n*-octane for further use. The synthesis yielded about 1.5 g of PbS QDs with a first exciton peak at 950 nm.

Synthesis of 1300 nm PbS QDs. In a three-neck flask, 2 mmol of lead oleate (1.54 g, 1.33 equiv) was dissolved in 20 mL of *n*-dodecane at 120 °C under a nitrogen atmosphere and flushed for 30 min. Next, 1.5 mmol of *N*-(p-(trifluoromethyl)phenyl)-*N*′-dodecylthiourea (0.5828 g, 1 equiv) was mixed with 1 mL of 1-methoxy-2-(2-methoxyethoxy)ethane or diglyme under a nitrogen atmosphere, preheated at 120 °C,

https://doi.org/10.1021/acsphotonics.3c00945
ACS Photonics XXXX, XXX, XXX−XXX

and quickly injected in the lead oleate solution at 120 °C. The reaction mixture was cooled down to room temperature by immersing the flask in a water bath after 80 s. The resulting dispersion was then purified at least four times with the aid of octane/acetone and finally passed through a 450 μm pore size syringe filter before redispersion in anhydrous *n*-octane and adjusting the desired concentration.

Fabrication of BI-QDPD. The ITO glass (Ossila) was ultrasonically cleaned with acetone, ethanol, and deionized water, followed by exposure to an O_2 plasma for 10 min. A ∼25 nm thick ZnO layer was deposited on the cleaned ITO substrate via spin-coating of the precursor solution. The samples were then annealed at 250 °C for 20 min in air. This step was repeated twice to get ∼50 nm of ZnO. Oleate-capped QDs are electrically insulating, and the ligands have to be replaced by shorter ligands. For the 1300 nm QDs, the long oleic acid (OA) was replaced by iodine via solution phase ligand exchange. 345 mg of PbI_2 (99.999%, Alfa Aesar), 110 mg of $PbBr_2$ (98%, Sigma-Aldrich), and 27 mg of NaOAc (99.999%, Sigma-Aldrich) were dissolved in 7.5 mL of N,N-dimethylformamide (DMF; anhydrous important, 98%, Sigma-Aldrich) in a 50 mL centrifuge tube. 5 mL solution of PbS-OA in *n*-octane (98%, Alfa Aesar) at a concentration of 5 mg/mL was then added to the exchange solution. The tube was vigorously shaken for 30 s to facilitate the transfer of the dot to the DMF phase. Subsequently, the *n*-octane phase was discarded. After the main exchange step, the remaining solution was washed three times with *n*-octane with a similar step. Subsequently, a 10-μL volume of butan-1-amine (BTA) (99%, Sigma-Aldrich) was added to the tubes to restabilize the colloid. Next, 6 mL (v/v 50%) of toluene was added to precipitate the QDs and the tubes were centrifuged at 2000 rpm for another 2 min. The QDs were then dried under vacuum for 3 min. The exchanged QD solid was dispersed in a solution of [BTA, amylamine, and hexylamine (volume ratio 10:3:2)] at the desired concentrations. Here, DMF was not used for dispersing the iodine-capped PbS QDs since it dissolved the photoresist (ARP672.08, Allresist) used for patterning the QD film during the integration.

Iodine-capped QDs were spin-coated on the ZnO layer at 2000 rpm for 30 s and annealed in N_2 for 10 min at 70 °C, forming the absorption layer with a thickness around 60 nm. Then 950 nm QDs were deposited on top by solid phase ligand exchange layer by layer. 50 mg/mL PbS-OA in *n*-octane solution was spun at 2500 rpm for 30 s. The EDT solution (0.01 vol % in methanol) was applied to the substrate for 30 s and spun at 2500 rpm for 10 s, followed by two-time methanol rinse. The 950 nm QDs deposition process was repeated twice to get a thickness of 60 nm. Methanol was used here instead of the more gentle solvent acetonitrile[70] since the latter swelled the photoresist. Finally, Au (120 nm) was thermally evaporated on the PbS film.

Waveguide Patterning. SiN was deposited on a silicon substrate with 3 μm thermal oxide in a plasma-enhanced chemical vapor deposition (PECVD) system (Advanced Vacuum Vision 310 PECVD) at 270 °C with N_2, NH_3 and SiH_4 chemistry. Before patterning the waveguides, we put some metal markers on the blank chip for better overlay alignment in the following patterning. The markers were patterned by using a 50 kV E-beam lithography (EBL) system (Voyager Raith), with a positive resist ARP6200.13 (∼400 nm, Allresist) and a dose of 200 $\mu C/cm^2$. The pattern was developed in *n*-amyl acetate for 60 s. Then the sample was moved to an E-gun evaporator (Leybold 560) for 5 nm Ti/100 nm Au/5 nm Ti. The thin layer of Ti was used to improve the adhesion. After metal evaporation, the sample was lifted off in resist remover AR600−71 (Allresist), with the help of sonication.

To pattern the waveguide, 400 nm ARP6200.13 E-beam resist was spun on the sample, followed by EBL with a dose of 160 $\mu C/cm^2$ and development in n-amyl acetate for 60 s. The resist pattern was transferred to SiN by reactive ion etching (RIE, Advanced Vacuum Vision 320) with CF_4 and H_2 chemistry. After etching, the resist was removed by immersing the sample in the resist remover AR600−71 for 10 min and in the O_2 plasma (PVA TePla 600) for 5 min. We then spin-coated the flowable oxide hydrogen silsesquioxane (HSQ, Dow FOX-15) on top of the sample as a top cladding layer. Diluted HSQ (HSQ: MIBK = 2:1) was spin-coated with a speed of 1300 rpm (acceleration 500 rpm/s), then baked on a hot plate at 150 °C for 2 min. To make the top cladding layer physically and chemically more stable, we cured the sample at 400 °C for 2 h in a N_2 atmosphere. After full curing, the thickness of the HSQ film goes down to ∼350 nm.

ALD of ZnO and Al_2O_3. Atomic layer deposition (ALD) was used to grow the ZnO electron transport layer. The depositions were performed in a custom-built ALD reactor with a base pressure of about 1×10^{-6} mbar. Prior to ALD growth, the samples were exposed to remote O_2 plasma (10 s, 3×10^{-3} mbar, at 200 W) to clean the sample surface due to air exposure. ZnO ALD was then performed using diethylzinc (>95%, Strem Chemicals, Inc.) as a precursor and deionized water as a coreactant at a deposition temperature of 150 °C. After depositing ca. 20 nm ZnO, ca. 10 nm Al_2O_3 was deposited on top with trimethylaluminum (>98%, Strem Chemicals, Inc.) as a precursor and deionized water as a coreactant at 150 °C. Al_2O_3 was used here as a protection layer, protecting ZnO from losing conductivity due to exposure to the O_2 plasma in the following fabrication. After ALD, the sample was annealed in a N_2 and H_2 atmosphere at 400 °C for 1 min to increase the conductivity of the ZnO layer.

N-Contact Patterning. Contact photolithography and lift-off were used to pattern the n-contact. Ti 35E (Microchemicals) photoresist was used in the image reversal tone to ease metal liftoff. Ti prime (Microchemicals) adhesion promotor was spun before photoresist to improve its adhesion with Al_2O_3. Adhesion promoter was important here, without which the ZnO and Al_2O_3 near the edge of the patterned resist will be attacked. After exposure, the sample was developed in diluted AZ400 K (buffered KOH, Microchemicals) solution (AZ400 K:H_2O = 1:3) for 5 min and 20 s. The resist was developed in 90 s, and the extra time was to remove the Al_2O_3 layer on top of ZnO. The etching time was critical since the KOH solution can also etch ZnO. Then the n-contact metal was evaporated, with a composition of 20 nm Ti/100 nm Au. Ti was used for low contact resistance with ZnO. After evaporation, the sample was immersed in an acetone puddle for 30 min and then rinsed with an acetone flow to lift off the metal on the photoresist. After liftoff, the sample was cleaned by exposing it to O_2 plasma for 5 min (PVA TePla 600).

ZnO Patterning. The ZnO layer was patterned by contact photolithography and chemical wet etching. Ti prime and Ti 35E were used again. After exposure, the sample was developed for 2 min in a diluted AZ400 K solution (AZ400 K:H_2O = 1:3). Then, the Al_2O_3 layer was locally removed using a AZ400 K:H2O = 1:10 solution and heated to 50 °C to fasten the

https://doi.org/10.1021/acsphotonics.3c00945
ACS Photonics XXXX, XXX, XXX−XXX

removal of Al_2O_3 and mitigate the photoresist attack. ZnO was removed by immersing the sample in a dilute HCl solution (37% HCl:H_2O = 1:50) for 30 s.

QD Patterning. The QD film was patterned by EBL and liftoff. PMMA (ARP672.08:anisole = 2:1, Allresist) was spin-coated with a speed of 3000 rpm (acceleration 1000 rpm/s) and baked at 150 °C for 3 min (thickness ∼400 nm). The PMMA was patterned using an exposure dose of 400 $\mu C/cm^2$ and development in AR600-55 (Allresist) for 90 s. Sonication was used during development to remove the undeveloped resist residue. PMMA resist was chosen here due to its good compatibility with the solvent methanol used during QDs deposition. Before depositing the QDs, the Al_2O_3 layer on top of ZnO was removed by immersing in dilute HCl solution (37% HCl:H_2O = 1:50) for 20s and buffered KOH solution (AZ400 K:H_2O = 1:40) at 50 °C for 1 min. Here, a dilute HCl solution was used to remove the residual Ti prime layer, which otherwise worked as an etching barrier. After the ZnO surface was exposed, PbS QDs (60 nm PbS-PbI and 60 nm PbS-EDT) were deposited on top with the same process as mentioned in the fabrication of the BI-QDPD. After the QD film deposition, the sample was lifted off in acetone for 10 min to finish the patterning of the QDs.

P-Contact Patterning. The p-contact was patterned by EBL and liftoff. PMMA (ARP672.08, Allresist) was spin-coated with a speed of 3000 rpm (acceleration 1000 rpm/s) and baked on a hot plate at 60 °C for 5 min. Then, the patterning area was exposed with a dose of 400 $\mu C/cm^2$ and developed in AR600-55 for 90 s with sonication. A low baking temperature was used to avoid increasing the dark current of the QDPDs. After development, the sample was coated with 100 nm of Au using an E-gun evaporator (Leybold), followed by a lift-off process in acetone for 30 min.

■ ASSOCIATED CONTENT

Supporting Information

The Supporting Information is available free of charge at https://pubs.acs.org/doi/10.1021/acsphotonics.3c00945.

Generation rate analysis and simulation and details on waveguide-coupled photodiode characterization (PDF)

■ AUTHOR INFORMATION

Corresponding Author

Dries Van Thourhout − *Photonics Research Group, Ghent University - imec, 9052 Ghent, Belgium; NB Photonics, Ghent University, 9052 Ghent, Belgium;* orcid.org/0000-0003-0111-431X; Email: Dries.VanThourhout@UGent.be

Authors

Chao Pang − *Photonics Research Group, Ghent University - imec, 9052 Ghent, Belgium; NB Photonics, Ghent University, 9052 Ghent, Belgium*

Yu-Hao Deng − *NB Photonics, Ghent University, 9052 Ghent, Belgium; Physics and Chemistry of Nanostructures Group, Ghent University, 9000 Ghent, Belgium*

Ezat Kheradmand − *NB Photonics, Ghent University, 9052 Ghent, Belgium; Physics and Chemistry of Nanostructures Group, Ghent University, 9000 Ghent, Belgium*

Nithin Poonkottil − *NB Photonics, Ghent University, 9052 Ghent, Belgium; Conformal Coating of Nanomaterials Group, Ghent University, 9000 Ghent, Belgium;* orcid.org/0000-0003-1360-1879

Robin Petit − *NB Photonics, Ghent University, 9052 Ghent, Belgium; Conformal Coating of Nanomaterials Group, Ghent University, 9000 Ghent, Belgium;* orcid.org/0000-0001-8488-3696

Lukas Elsinger − *Photonics Research Group, Ghent University - imec, 9052 Ghent, Belgium; NB Photonics, Ghent University, 9052 Ghent, Belgium;* orcid.org/0000-0001-9427-750X

Christophe Detavernier − *NB Photonics, Ghent University, 9052 Ghent, Belgium; Conformal Coating of Nanomaterials Group, Ghent University, 9000 Ghent, Belgium*

Pieter Geiregat − *NB Photonics, Ghent University, 9052 Ghent, Belgium; Physics and Chemistry of Nanostructures Group, Ghent University, 9000 Ghent, Belgium;* orcid.org/0000-0001-7217-8738

Zeger Hens − *NB Photonics, Ghent University, 9052 Ghent, Belgium; Physics and Chemistry of Nanostructures Group, Ghent University, 9000 Ghent, Belgium;* orcid.org/0000-0002-7041-3375

Complete contact information is available at: https://pubs.acs.org/10.1021/acsphotonics.3c00945

Funding

D.V.T., Z.H., and P.G. acknowledge FWO-Vlaanderen for research funding (FWO projects G0B2921N and G0C5723N). Z.H. and C.D. acknowledge Ghent University for funding (BOF-GOA01019). C.P. would like to acknowledge the China Scholarship Council (CSC Grant 201906120023) for PhD support. The work received funding from the European Research Council (ERC) under the innovation program grant agreement No. 884963 (ERC AdG NARIOS).

Notes

The authors declare no competing financial interest.

■ ACKNOWLEDGMENTS

The authors would like to thank Steven Verstuyft, Muhammad Muneeb, Liesbet Van Landschoot, and Clemens Krückel for their technical assistance during this research.

■ REFERENCES

(1) Pradhan, S.; Di Stasio, F.; Bi, Y.; Gupta, S.; Christodoulou, S.; Stavrinadis, A.; Konstantatos, G. High-Efficiency Colloidal Quantum Dot Infrared Light-Emitting Diodes via Engineering at the Supra-Nanocrystalline Level. *Nat. Nanotechnol.* **2019**, *14* (1), 72−79.

(2) Dai, X.; Zhang, Z.; Jin, Y.; Niu, Y.; Cao, H.; Liang, X.; Chen, L.; Wang, J.; Peng, X. Solution-Processed, High-Performance Light-Emitting Diodes Based on Quantum Dots. *Nature* **2014**, *515* (7525), 96−99.

(3) Klimov, V. I.; Mikhailovsky, A. A.; Xu, S.; Malko, A.; Hollingsworth, J. A.; Leatherdale, C. A.; Eisler, H. J.; Bawendi, M. G. Optical Gain and Stimulated Emission in Nanocrystal Quantum Dots. *Science* **2000**, *290* (5490), 314−317.

(4) Xie, W.; Stöferle, T.; Rainò, G.; Aubert, T.; Bisschop, S.; Zhu, Y.; Mahrt, R. F.; Geiregat, P.; Brainis, E.; Hens, Z.; Van Thourhout, D. On-Chip Integrated Quantum-Dot−Silicon-Nitride Microdisk Lasers. *Adv. Mater.* **2017**, *29* (16), 2−7.

(5) Park, Y. S.; Roh, J.; Diroll, B. T.; Schaller, R. D.; Klimov, V. I. Colloidal Quantum Dot Lasers. *Nat. Rev. Mater.* **2021**, *6*, 382−401.

(6) Chuang, C. H. M.; Brown, P. R.; Bulović, V.; Bawendi, M. G. Improved Performance and Stability in Quantum Dot Solar Cells through Band Alignment Engineering. *Nat. Mater.* **2014**, *13* (8), 796−801.

(7) Vafaie, M.; Fan, J. Z.; Morteza Najarian, A.; Ouellette, O.; Sagar, L. K.; Bertens, K.; Sun, B.; García de Arquer, F. P.; Sargent, E. H.

Colloidal Quantum Dot Photodetectors with 10-Ns Response Time and 80% Quantum Efficiency at 1,550 Nm. *Matter* **2021**, *4* (3), 1042−1053.
(8) Georgitzikis, E.; Malinowski, P. E.; Maes, J.; Hadipour, A.; Hens, Z.; Heremans, P.; Cheyns, D. Optimization of Charge Carrier Extraction in Colloidal Quantum Dots Short-Wave Infrared Photodiodes through Optical Engineering. *Adv. Funct. Mater.* **2018**, *28* (42), No. 1804502.
(9) Kagan, C. R.; Lifshitz, E.; Sargent, E. H.; Talapin, D. V. Building Devices from Colloidal Quantum Dots. *Science* **2016**, *353* (6302), 5523.
(10) Choi, M. K.; Yang, J.; Hyeon, T.; Kim, D. H. Flexible Quantum Dot Light-Emitting Diodes for next-Generation Displays. *npj Flex Electron.* **2018**, *2* (1), 10.
(11) Chen, H.; He, J.; Wu, S. Recent Advances on Quantum-Dot-Enhanced Liquid-Crystal. *Displays* **2017**, *23*, 5.
(12) Liu, Z.; Lin, C. H.; Hyun, B. R.; Sher, C. W.; Lv, Z.; Luo, B.; Jiang, F.; Wu, T.; Ho, C. H.; Kuo, H. C.; He, J. H. Micro-Light-Emitting Diodes with Quantum Dots in Display Technology. *Light Sci. Appl.* **2020**, *9* (1), 83.
(13) Wood, V.; Panzer, M. J.; Caruge, J.-M.; Halpert, J. E.; Bawendi, M. G.; Bulović, V. B. Air-Stable Operation of Transparent, Colloidal Quantum Dot Based LEDs with a Unipolar Device. *Architecture* **2010**, *10*, 24−29.
(14) Yang, J.; Choi, M. K.; Yang, U. J.; Kim, S. Y.; Kim, Y. S.; Kim, J. H.; Kim, D. H.; Hyeon, T. Toward Full-Color Electroluminescent Quantum Dot Displays. *Nano Lett.* **2021**, *21* (1), 26−33.
(15) Gregory, C.; Hilton, A.; Violette, K.; Klem, E. J. D. Colloidal Quantum Dot Photodetectors for Large Format Nir, Swir, and Eswir Imaging Arrays. *Dig. Technol. Pap. - SID Int. Symp.* **2021**, *52* (1), 982−986.
(16) Pejovic, V.; Lee, J.; Georgitzikis, E.; Li, Y.; Kim, J. H.; Lieberman, I.; Malinowski, P. E.; Heremans, P.; Cheyns, D. Thin-Film Photodetector Optimization for High-Performance Short-Wavelength Infrared Imaging. *IEEE Electron Device Lett.* **2021**, *42* (8), 1196−1199.
(17) Bowers, J. E.; Liu, A. Y. A Comparison of Four Approaches to Photonic Integration. *Opt. InfoBase Conf. Pap.* **2017**, 2−4.
(18) Kaur, P.; Boes, A.; Ren, G.; Nguyen, T. G.; Roelkens, G.; Mitchell, A. Hybrid and Heterogeneous Photonic Integration. *APL Photonics* **2021**, *6* (6), 52700.
(19) Komljenovic, T.; Davenport, M.; Hulme, J.; Liu, A. Y.; Santis, C. T.; Spott, A.; Srinivasan, S.; Stanton, E. J.; Zhang, C.; Bowers, J. E. Heterogeneous Silicon Photonic Integrated Circuits. *J. Light. Technol.* **2016**, *34* (1), 20−35.
(20) Roelkens, G.; Zhang, J.; Bogaert, L.; Billet, M.; Wang, D.; Pan, B.; Kruckel, C. J.; Soltanian, E.; Maes, D.; Vanackere, T.; Vandekerckhove, T.; Cuyvers, S.; De Witte, J.; Lufungula, I. L.; Guo, X.; Li, H.; Qin, S.; Muliuk, G.; Uvin, S.; Haq, B.; Op De Beeck, C.; Goyvaerts, J.; Lepage, G.; Verheyen, P.; Van Campenhout, J.; Morthier, G.; Kuyken, B.; Van Thourhout, D.; Baets, R. Micro-Transfer Printing for Heterogeneous Si Photonic Integrated Circuits. *IEEE J. Sel. Top. Quantum Electron.* **2023**, *29* (3), No. 3222686.
(21) Corbett, B.; Loi, R.; O'Callaghan, J.; Roelkens, G. Transfer Printing for Silicon Photonics. *Semicond. Semimetals* **2018**, *99*, 43−70.
(22) Baets, R.; Subramanian, A. Z.; Clemmen, S.; Kuyken, B.; Bienstman, P.; Le Thomas, N.; Roelkens, G.; Van Thourhout, D.; Helin, P.; Severi, S. Silicon Photonics: Silicon Nitride versus Silicon-on-Insulator. *2016 Opt. Fiber Commun. Conf. Exhib. OFC 2016* **2016**, 3−5.
(23) Poulton, C. V.; Byrd, M. J.; Raval, M.; Su, Z.; Li, N.; Timurdogan, E.; Coolbaugh, D.; Vermeulen, D.; Watts, M. R. Large-Scale Silicon Nitride Nanophotonic Phased Arrays at Infrared and Visible Wavelengths. *Opt. Lett.* **2017**, *42* (1), 21.
(24) Tyler, N. A.; Fowler, D.; Malhouitre, S.; Garcia, S.; Grosse, P.; Rabaud, W.; Szelag, B. SiN Integrated Optical Phased Arrays for Two-Dimensional Beam Steering at a Single near-Infrared Wavelength. *Opt. Express* **2019**, *27* (4), 5851.
(25) Zadka, M.; Chang, Y.-C.; Mohanty, A.; Phare, C. T.; Roberts, S. P.; Lipson, M. On-Chip Platform for a Phased Array with Minimal Beam Divergence and Wide Field-of-View. *Opt. Express* **2018**, *26* (3), 2528.
(26) Antonacci, G.; Goyvaerts, J.; Zhao, H.; Baumgartner, B.; Lendl, B.; Baets, R. Ultra-Sensitive Refractive Index Gas Sensor with Functionalized Silicon Nitride Photonic Circuits. *APL Photonics* **2020**, *5* (8), 13577.
(27) Peyskens, F.; Wuytens, P.; Raza, A.; Van Dorpe, P.; Baets, R. Waveguide Excitation and Collection of Surface-Enhanced Raman Scattering from a Single Plasmonic Antenna. *Nanophotonics* **2018**, *7* (7), 1299−1306.
(28) Subramanian, A. Z.; Ryckeboer, E.; Dhakal, A.; Peyskens, F.; Malik, A.; Kuyken, B.; Zhao, H.; Pathak, S.; Ruocco, A.; De Groote, A.; Wuytens, P.; Martens, D.; Leo, F.; Xie, W.; Dave, U. D.; Muneeb, M.; Van Dorpe, P.; Van Campenhout, J.; Bogaerts, W.; Bienstman, P.; Le Thomas, N.; Van Thourhout, D.; Hens, Z.; Roelkens, G.; Baets, R. Silicon and Silicon Nitride Photonic Circuits for Spectroscopic Sensing On-a-Chip [Invited]. *Photonics Res.* **2015**, *3* (5), B47.
(29) Taballione, C.; Wolterink, T. A. W.; Lugani, J.; Eckstein, A.; Bell, B. A.; Grootjans, R.; Visscher, I.; Renema, J. J.; Geskus, D.; Roeloffzen, C. G. H.; Walmsley, I. A.; Pinkse, P. W. H.; Boller, K. J. 8 × 8 Programmable Quantum Photonic Processor Based on Silicon Nitride Waveguides. *Opt. InfoBase Conf. Pap.* **2018**, No. 19, 22−24.
(30) Senichev, A.; Peana, S.; Martin, Z. O.; Yesilyurt, O.; Sychev, D.; Lagutchev, A. S.; Boltasseva, A.; Shalaev, V. M. Silicon Nitride Waveguides with Intrinsic Single-Photon Emitters for Integrated Quantum Photonics. *ACS Photonics* **2022**, *9* (10), 3357−3365.
(31) Moody, G.; Sorger, V. J.; Blumenthal, D. J.; Juodawlkis, P. W.; Loh, W.; Sorace-Agaskar, C.; Jones, A. E.; Balram, K. C.; Matthews, J. C. F.; Laing, A.; Davanco, M.; Chang, L.; Bowers, J. E.; Quack, N.; Galland, C.; Aharonovich, I.; Wolff, M. A.; Schuck, C.; Sinclair, N.; Lončar, M.; Komljenovic, T.; Weld, D.; Mookherjea, S.; Buckley, S.; Radulaski, M.; Reitzenstein, S.; Pingault, B.; Machielse, B.; Mukhopadhyay, D.; Akimov, A.; Zheltikov, A.; Agarwal, G. S.; Srinivasan, K.; Lu, J.; Tang, H. X.; Jiang, W.; McKenna, T. P.; Safavi-Naeini, A. H.; Steinhauer, S.; Elshaari, A. W.; Zwiller, V.; Davids, P. S.; Martinez, N.; Gehl, M.; Chiaverini, J.; Mehta, K. K.; Romero, J.; Lingaraju, N. B.; Weiner, A. M.; Peace, D.; Cernansky, R.; Lobino, M.; Diamanti, E.; Vidarte, L. T.; Camacho, R. M. 2022 Roadmap on Integrated Quantum Photonics. *J. Phys. Photonics* **2022**, *4*, 1.
(32) Zhu, Y.; Xie, W.; Bisschop, S.; Aubert, T.; Brainis, E.; Geiregat, P.; Hens, Z.; Van Thourhout, D. On-Chip Single-Mode Distributed Feedback Colloidal Quantum Dot Laser under Nanosecond Pumping. *ACS Photonics* **2017**, *4* (10), 2446−2452.
(33) Cegielski, P. J.; Giesecke, A. L.; Neutzner, S.; Porschatis, C.; Gandini, M.; Schall, D.; Perini, C. A. R.; Bolten, J.; Suckow, S.; Kataria, S.; Chmielak, B.; Wahlbrink, T.; Petrozza, A.; Lemme, M. C. Monolithically Integrated Perovskite Semiconductor Lasers on Silicon Photonic Chips by Scalable Top-Down Fabrication. *Nano Lett.* **2018**, *18* (11), 6915−6923.
(34) Xie, W.; Gomes, R.; Aubert, T.; Bisschop, S.; Zhu, Y.; Hens, Z.; Brainis, E.; Van Thourhout, D. Nanoscale and Single-Dot Patterning of Colloidal Quantum Dots. *Nano Lett.* **2015**, *15* (11), 7481−7487.
(35) Chen, Y.; Ryou, A.; Friedfeld, M. R.; Fryett, T.; Whitehead, J.; Cossairt, B. M.; Majumdar, A. Deterministic Positioning of Colloidal Quantum Dots on Silicon Nitride Nanobeam Cavities. *Nano Lett.* **2018**, *18* (10), 6404−6410.
(36) Xie, W.; Zhu, Y.; Bisschop, S.; Aubert, T.; Hens, Z.; Van Thourhout, D.; Geiregat, P. Colloidal Quantum Dots Enabling Coherent Light Sources for Integrated Silicon-Nitride Photonics. *IEEE J. Sel. Top. Quantum Electron.* **2017**, *23* (5), No. 2737882.
(37) Yu, Q.; Gao, J.; Ye, N.; Chen, B.; Sun, K.; Xie, L.; Srinivasan, K.; Zervas, M.; Navickaite, G.; Geiselmann, M.; Beling, A. Heterogeneous Photodiodes on Silicon Nitride Waveguides with 20 GHz Bandwidth. *Opt. InfoBase Conf. Pap.* **2020**, No. 10, 14824−14831.
(38) Goyvaerts, J.; Kumari, S.; Uvin, S.; Zhang, J.; Baets, R.; Gocalinska, A.; Pelucchi, E.; Corbett, B.; Roelkens, G. Transfer-Print Integration of GaAs p-i-n Photodiodes onto Silicon Nitride Photonic

https://doi.org/10.1021/acsphotonics.3c00945
ACS Photonics XXXX, XXX, XXX−XXX

Integrated Circuits. *2020 IEEE Photonics Conf. IPC 2020 - Proc.* **2020**, *28* (14), 21275−21285.
(39) Jung, B. K.; Woo, H. K.; Shin, C.; Park, T.; Li, N.; Lee, K. J.; Kim, W.; Bae, J. H.; Ahn, J. P.; Ng, T. N.; Oh, S. J. Suppressing the Dark Current in Quantum Dot Infrared Photodetectors by Controlling Carrier Statistics. *Adv. Opt. Mater.* **2022**, *10* (2), No. 2101611.
(40) Killilea, N.; Wu, M.; Sytnyk, M.; Yousefi Amin, A. A.; Mashkov, O.; Spiecker, E.; Heiss, W. Pushing PbS/Metal-Halide-Perovskite Core/Epitaxial-Ligand-Shell Nanocrystal Photodetectors beyond 3 Mm Wavelength. *Adv. Funct. Mater.* **2019**, *29* (14), No. 1807964.
(41) Elsinger, L.; Petit, R.; Van Acker, F.; Zawacka, N. K.; Tanghe, I.; Neyts, K.; Detavernier, C.; Geiregat, P.; Hens, Z.; Van Thourhout, D. Waveguide-Coupled Colloidal Quantum Dot Light Emitting Diodes and Detectors on a Silicon Nitride Platform. *Laser Photonics Rev.* **2021**, *15* (7), 230.
(42) Bothra, U.; Albaladejo-Siguan, M.; Vaynzof, Y.; Kabra, D. Impact of Ligands on the Performance of PbS Quantum Dot Visible−Near-Infrared Photodetectors. *Adv. Opt. Mater.* **2023**, *11* (1), No. 2201897.
(43) Parmar, D. H.; M. Pina, J.; Zhu, T.; Vafaie, M.; Atan, O.; Biondi, M.; Najjariyan, A. M.; Hoogland, S.; Sargent, E. H. Controlled Crystal Plane Orientations in the ZnO Transport Layer Enable High-Responsivity, Low-Dark-Current Infrared Photodetectors. *Adv. Mater.* **2022**, *34* (17), No. e2200321.
(44) You, H. R.; Park, J. Y.; Lee, D. H.; Kim, Y.; Choi, J. Recent Research Progress in Surface Ligand Exchange of PbS Quantum Dots for Solar Cell Application. *Appl. Sci.* **2020**, *10* (3), 30975.
(45) Ning, Z.; Voznyy, O.; Pan, J.; Hoogland, S.; Adinolfi, V.; Xu, J.; Li, M.; Kirmani, A. R.; Sun, J. P.; Minor, J.; Kemp, K. W.; Dong, H.; Rollny, L.; Labelle, A.; Carey, G.; Sutherland, B.; Hill, I.; Amassian, A.; Liu, H.; Tang, J.; Bakr, O. M.; Sargent, E. H. Air-Stable n-Type Colloidal Quantum Dot Solids. *Nat. Mater.* **2014**, *13* (8), 822−828.
(46) Bogaerts, W.; Li, Y.; Pathak, S.; Ruocco, A.; Fiers, M.; Ribeiro, A.; Lambert, E.; Dumon, P. Integrated Design for Integrated Photonics: From the Physical to the Circuit Level and Back. *Integr. Opt. Phys. Simul.* **2013**, *8781*, 878102.
(47) Piels, M.; Bauters, J. F.; Davenport, M. L.; Heck, M. J. R.; Bowers, J. E. Low-Loss Silicon Nitride AWG Demultiplexer. *J. Light. Technol.* **2014**, *32* (4), 817−823.
(48) Martens, D.; Subramanian, A. Z.; Pathak, S.; Vanslembrouck, M.; Bienstman, P.; Bogaerts, W.; Baets, R. G. Compact Silicon Nitride Arrayed Waveguide Gratings for Very Near-Infrared Wavelengths. *IEEE Photonics Technol. Lett.* **2015**, *27* (2), 137−140.
(49) Pathak, S.; Vanslembrouck, M.; Dumon, P.; Van Thourhout, D.; Bogaerts, W. Optimized Silicon Awg with Flattened Spectral Response Using an MMI Aperture. *J. Light. Technol.* **2013**, *31* (1), 87−93.
(50) Ben Mohammadi, L.; Klotzbuecher, T.; Sigloch, S.; Welzel, K.; Göddel, M.; Pieber, T. R.; Schaupp, L. In Vivo Evaluation of a Chip Based near Infrared Sensor for Continuous Glucose Monitoring. *Biosens. Bioelectron.* **2014**, *53*, 99−104.
(51) Ryckeboer, E.; Bockstaele, R.; Vanslembrouck, M.; Baets, R. Glucose Sensing by Waveguide-Based Absorption Spectroscopy on a Silicon Chip. *Biomed. Opt. Express* **2014**, *5* (5), 1636.
(52) Trita, A.; Voet, E.; Vermeiren, J.; Delbeke, D.; Dumon, P.; Pathak, S.; Van Thourhout, D. Simultaneous Interrogation of Multiple Fiber Bragg Grating Sensors Using an Arrayed Waveguide Grating Filter Fabricated in SOI Platform. *IEEE Photonics J.* **2015**, *7* (6), No. 2499546.
(53) Maes, D.; Lemey, S.; Roelkens, G.; Zaknoune, M.; Avramovic, V.; Okada, E.; Szriftgiser, P.; Peytavit, E.; Ducournau, G.; Kuyken, B. High-Speed Uni-Traveling-Carrier Photodiodes on Silicon Nitride. *APL Photonics* **2023**, *8* (1), No. 016104.
(54) Lischke, S.; Fraschke, M.; Richter, H.; Kruger, A.; Saarow, U.; Heinrich, P.; Winzer, G.; Schulz, K.; Kulse, P.; Trusch, A.; Zimmermann, L.; Knoll, D.; Mai, C.; Hesse, A.; Georgieva, G.; Peczek, A.; Kroh, A.; Lisker, M.; Schmidt, D. Silicon Nitride Waveguide Coupled 67+ GHz Ge Photodiode for Non-SOI PIC and EPIC Platforms. *Technol. Dig. - Int. Electron Devices Meet. IEDM* **2019**, 779−782.
(55) Sacher, W. D.; Mikkelsen, J. C.; Huang, Y.; Mak, J. C. C.; Yong, Z.; Luo, X.; Li, Y.; Dumais, P.; Jiang, J.; Goodwill, D.; Bernier, E.; Lo, P. G. Q.; Poon, J. K. S. Monolithically Integrated Multilayer Silicon Nitride-on-Silicon Waveguide Platforms for 3-D Photonic Circuits and Devices. *Proc. IEEE* **2018**, *106* (12), 2232−2245.
(56) Gonzalez Marin, J. F.; Unuchek, D.; Watanabe, K.; Taniguchi, T.; Kis, A. MoS_2 Photodetectors Integrated with Photonic Circuits. *npj 2D Mater. Appl.* **2019**, *3*, 14.
(57) Gherabli, R.; Indukuri, S. R. K. C.; Zektzer, R.; Frydendahl, C.; Levy, U. $MoSe_2/WS_2$ Heterojunction Photodiode Integrated with a Silicon Nitride Waveguide for near Infrared Light Detection with High Responsivity. *Light Sci. Appl.* **2023**, *12*, 60.
(58) Salamin, Y.; Ma, P.; Baeuerle, B.; Emboras, A.; Fedoryshyn, Y.; Heni, W.; Cheng, B.; Josten, A.; Leuthold, J. 100 GHz Plasmonic Photodetector. *ACS Photonics* **2018**, *5* (8), 3291−3297.
(59) Ahn, G. H.; White, A. D.; Kim, H.; Higashitarumizu, N.; Mayor, F. M.; Herrmann, J. F.; Jiang, W.; Multani, K. K. S.; Safavi-Naeini, A. H.; Javey, A.; Vučković, J. Platform-Agnostic Waveguide Integration of High-Speed Photodetectors with Evaporated Tellurium Thin Films. *Optica* **2023**, *10* (3), 349.
(60) Yu, Q.; Gao, J.; Ye, N.; Chen, B.; Sun, K.; Xie, L.; Srinivasan, K.; Zervas, M.; Navickaite, G.; Geiselmann, M. Heterogeneous Photodiodes on Silicon Nitride Waveguides. *Opt. Express* **2020**, *28* (10), 14824−14830.
(61) Rahman, F.; Carbaugh, D. J.; Wright, J. T.; Rajan, P.; Pandya, S. G.; Kaya, S. A Review of Polymethyl Methacrylate (PMMA) as a Versatile Lithographic Resist − With Emphasis on UV Exposure. *Microelectron. Eng.* **2020**, *224*, No. 111238.
(62) Carbaugh, D. J.; Wright, J. T.; Parthiban, R.; Rahman, F. Photolithography with Polymethyl Methacrylate (PMMA). *Semicond. Sci. Technol.* **2016**, *31* (2), No. 025010.
(63) Keuleyan, S.; Lhuillier, E.; Brajuskovic, V.; Guyot-Sionnest, P. Mid-Infrared HgTe Colloidal Quantum Dot Photodetectors. *Nat. Photonics* **2011**, *5* (8), 489−493.
(64) Ackerman, M. M.; Tang, X.; Guyot-Sionnest, P. Fast and Sensitive Colloidal Quantum Dot Mid-Wave Infrared Photodetectors. *ACS Nano* **2018**, *12* (7), 7264−7271.
(65) Roelkens, G.; Dave, U.; Gassenq, A.; Hattasan, N.; Hu, C.; Kuyken, B.; Leo, F.; Malik, A.; Muneeb, M.; Ryckeboer, E.; Sanchez, D.; Uvin, S.; Wang, R.; Hens, Z.; Baets, R.; Shimura, Y.; Gencarelli, F.; Vincent, B.; Loo, R.; Van Campenhout, J.; Cerutti, L.; Rodriguez, J. B.; Tournie, E.; Chen, X.; Nedeljkovic, M.; Mashanovich, G.; Shen, L.; Healy, N.; Peacock, A. C.; Liu, X.; Osgood, R.; Green, W. M. J. Silicon-Based Photonic Integration beyond the Telecommunication Wavelength Range. *IEEE J. Sel. Top. Quantum Electron.* **2014**, *20* (4), 2294460.
(66) Marris-Morini, D.; Vakarin, V.; Ramirez, J. M.; Liu, Q.; Ballabio, A.; Frigerio, J.; Montesinos, M.; Alonso-Ramos, C.; Le Roux, X.; Serna, S.; Benedikovic, D.; Chrastina, D.; Vivien, L.; Isella, G. Germanium-Based Integrated Photonics from near- to Mid-Infrared Applications. *Nanophotonics* **2018**, *7* (11), 1781−1793.
(67) Liow, T. Y.; Ang, K. W.; Fang, Q.; Song, J. F.; Xiong, Y. Z.; Yu, M. Bin; Lo, G. Q.; Kwong, D. L. Silicon Modulators and Germanium Photodetectors on SOI: Monolithic Integration, Compatibility, and Performance Optimization. *IEEE J. Sel. Top. Quantum Electron.* **2010**, *16* (1), 307−315.
(68) Bao, J.; Bawendi, M. G. A Colloidal Quantum Dot Spectrometer. *Nature* 2015, *523* (7558), 67−70, DOI: 10.1038/nature14576.
(69) Hendricks, M. P.; Campos, M. P.; Cleveland, G. T.; Plante, I. J. La; Owen, J. S. A Tunable Library of Substituted Thiourea Precursors to Metal Sulfide Nanocrystals. *Science* **2015**, *348* (6240), 1226−1230.
(70) Kirmani, A. R.; Carey, G. H.; Abdelsamie, M.; Yan, B.; Cha, D.; Rollny, L. R.; Cui, X.; Sargent, E. H.; Amassian, A. Effect of Solvent Environment on Colloidal-Quantum-Dot Solar-Cell Manufacturability and Performance. *Adv. Mater.* **2014**, *26* (27), 4717−4723.

https://doi.org/10.1021/acsphotonics.3c00945
ACS Photonics XXXX, XXX, XXX−XXX